Earth Planet. Sci. Lett. 651 (2025) 119171

Contents lists available at ScienceDirect

Earth and Planetary Science Letters

journal homepage: www.elsevier.com/locate/epsl

Rheology of hydrous minerals in the subduction multisystem

Charis M. Horn, Philip Skemer *

Department of Earth, Environmental, and Planetary Sciences, Washington University in St. Louis, USA

ARTICLE INFO

Editor: Carolina Lithgow-Bertelloni

Keywords:
Hydrous minerals
Nanoindentation
Subduction
Rheology

ABSTRACT

The relatively low strength of the hydrous minerals has been theorized to play a role in the initiation of subduction through the feedbacks between faulting, hydration reactions, and rheological weakening. To further explore the behaviour of hydrous magnesium silicate minerals under the high stress conditions relevant to propagating faults, we performed nanoindentation tests on three serpentine species—lizardite, antigorite, and chrysotile—from room temperature up to their respective dehydration temperatures. While all serpentine minerals exhibit markedly lower indentation hardness than olivine under the same conditions (H_{ol} = 13.1–14.9 GPa), we find that antigorite (H_{atg} = 5.7–6.7 GPa) is almost a factor of three harder than lizardite (H_{liz} = 2.2–2.6 GPa), which is itself an order of magnitude harder than chrysotile (H_{ctl} = 0.1 GPa). We also indented chlorite from room temperature up to 400 °C and found that it has a hardness between that of lizardite and antigorite (H_{chl} = 2.8–4.0 GPa). Chrysotile is even weaker than the mineral talc (H_{tlc} = 0.6 GPa), another hydrous magnesium silicate, which was tested in a previous study. The weakest hydrous magnesium silicates – talc and chrysotile – are approximately one order of magnitude weaker than antigorite and almost two orders of magnitude weaker than olivine. There is a systematic relationship between indentation hardness and the lattice spacing between c-planes in these sheet silicates. Geodynamic models of subduction initiation typically use an ad hoc finite yield stress to trigger localized deformation. This study confirms that hydrous magnesium silicates are a likely candidate for alteration products that can facilitate localized deformation both before and after subduction initiation. However, the degree of weakening is highly dependent on the specific reaction product.

1. Introduction

Hydrous magnesium silicates such as the serpentine group minerals ($Mg_3Si_2O_5(OH)_4$), chlorite ($(Mg_5Al)(Si_3Al)O_{10}(OH)_8$), and talc ($Mg_3Si_4O_{10}(OH)_2$) form primarily by the hydration of lithospheric rocks of mafic and ultramafic composition, and are fundamentally important to the subduction zone multisystem (Evans et al., 1976). As major water carriers, they are likely responsible for a large portion of the H_2O flux into the mantle (Parai and Mukhopadhyay, 2012; Pawley, 2003; Rüpke et al., 2004), with associated implications for the global water cycle and the induction of volcanic melting beneath arcs. Additionally, prior experimental work on the serpentine group has indicated that these minerals and other phyllosilicates may be rheologically weaker than average oceanic crust (Amiguet et al., 2012; Hilairet et al., 2007), consistent with observations of highly deformed serpentinites in naturally exhumed subduction materials (Horn et al., 2020; Raleigh and Paterson, 1965). Since low yield strength materials are required to generate plate-like tectonic behaviour in numerical models (e.g. Dymkova and Gerya, 2013; Nikolaeva et al., 2010; Toth and Gurnis, 1998), hydrous magnesium silicates are widely theorized to be viable candidates for both the initiation of localized deformation and the stability of subduction zones (e.g. Reynard, 2013; Stern and Gerya, 2018).

The different minerals that make up the serpentine system are distinguished by the morphology of the sheets that characterise the crystal structure (Evans, 2004). Lizardite, stable at low temperatures and the most abundant serpentine phase in the shallow upper mantle (Wicks and Whittaker, 1977), is composed of parallel sheets stacked on top of one another and is similar in structure to chlorite and talc (Amiguet et al., 2012). Antigorite, the high pressure, high temperature variety of the serpentine group, has a more complicated structure comprised of crenulated sheets (Mével, 2003). Rheological dissimilarities between the two species, inferred to be a result of their differing crystallography, have been confirmed in prior experimental work (Hirauchi and Katayama, 2013). Finally, chrysotile has a more unusual structure in which the otherwise planar sheets are coiled into fibres (Whittaker, 1957). Within this group of hydrous magnesium silicate

* Corresponding author at: Rudolph Hall Room 110, Washington University in St. Louis, 1 Brookings Drive, St. Louis, MO 63130 USA.
E-mail address: pskemer@wustl.edu (P. Skemer).

https://doi.org/10.1016/j.epsl.2024.119171
Received 1 March 2024; Received in revised form 18 November 2024; Accepted 7 December 2024

minerals there are still many unknowns, particularly with regards to precise deformation mechanisms, rheological behaviour, relative mechanical properties, and stability fields (Amiguet et al., 2014, 2012).

Previous experimental studies of serpentine group rheology used solid medium D-DIA or fluid medium Griggs-type apparatuses to generate high confining pressures, and determined flow stresses using either diffracted x-rays at a synchrotron beamline or fitting instrumental stress and strain-rate data using a Markov Chain Monte-Carlo fitting method (Amiguet et al., 2012; Burdette and Hirth, 2022; Hilairet et al., 2007). In this study, we seek to complement these previous efforts by performing nanoindentation tests on all three serpentine species plus chlorite, and comparing these results with our previous study on talc (Horn and Skemer, 2023). The objective is to assess the relative yield stresses of hydrous magnesium silicates under high stress conditions relevant to crack tips during seismic and aseismic rupture (e.g. Rice, 1992).

2. Methods

2.1. Starting materials and sample preparation

Natural samples of the three main varieties of serpentinite – antigorite, lizardite, and chrysotile – as well as a specimen of chlorite (var: clinochlore), were selected for analysis (Fig. 1). Antigorite serpentinite (sample "GC" from Reinen et al., 1994) was determined to have a composition of $Mg_{2.8}Fe_{0.1}Al_{0.1}Si_2O_5(OH)_4$ using the JEOL JXA-8200 electron microprobe in the Department of Earth, Environmental, and Planetary Sciences at Washington University in St. Louis. The specimen is composed of needle-like grains of antigorite that are approximately 100 μm x 30 μm in size. Optical microscopy of the antigorite serpentinite

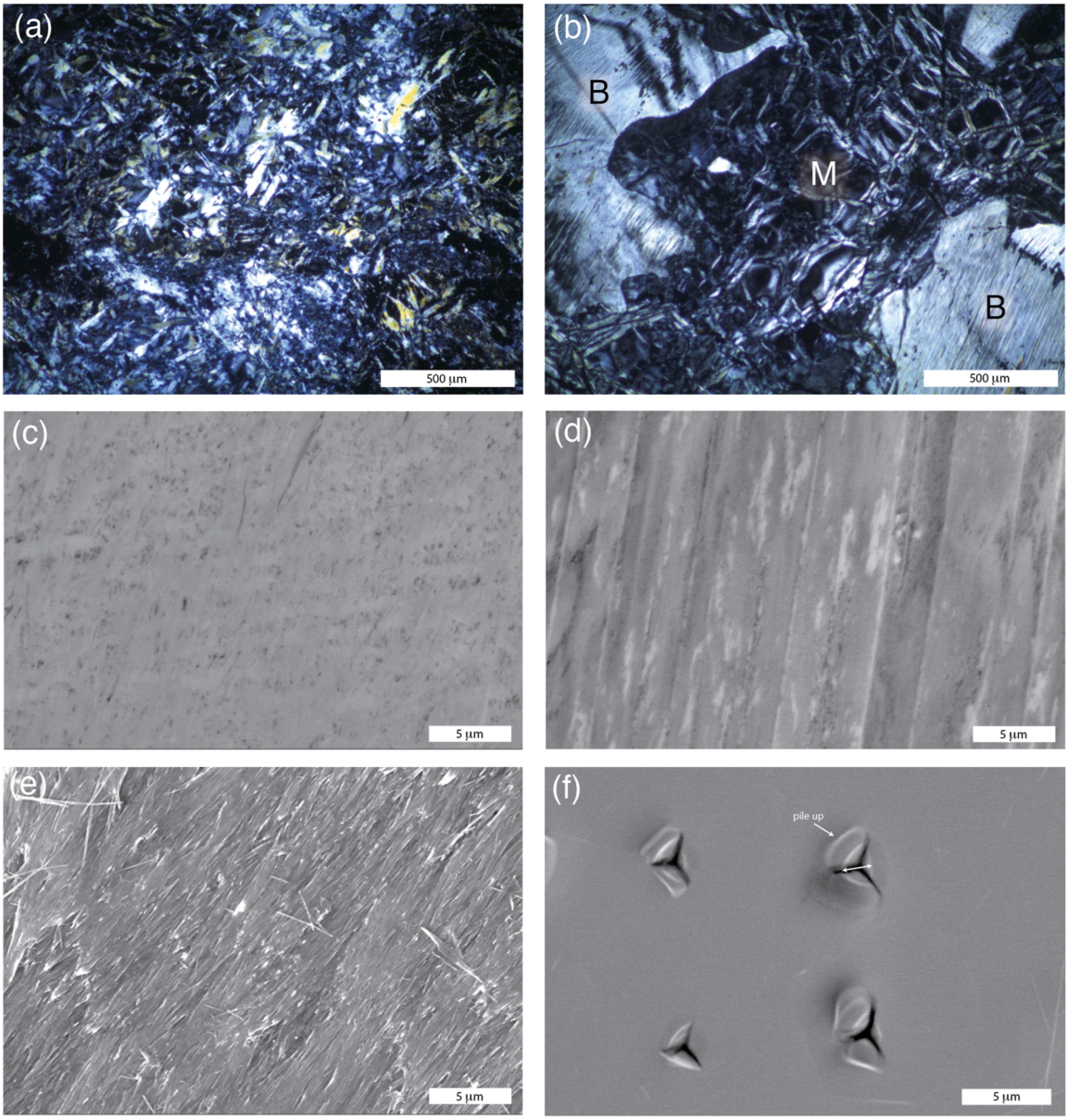

Fig. 1. Micrographs of serpentine and chlorite samples under crossed polarised light (a, b) and with secondary electron imaging (c,d,e,f), showing their respective microstructures. Antigorite (a,c) is composed of long, interlocking grains that meet at high angles. Lizardite (b,d) is arranged in both mesh cells (M) and bastites (B). Chrysotile (e) exhibits the characteristic fibrous texture with resolvable fibres that tens of nm in diameter. (f) shows an array of indents, made a room temperature, in a single crystal of chlorite. The indents are pyramidal, reflecting the shape of the Bercovich indenter. The double-sided arrow shows the extent of one indent, from a corner to a face. Pile-up, caused by material displaced by the indenter, is seen along the perimeter. There is no evidence for cracks radiating for the corners of the indents, which is expected if brittle deformation occurs.

reveals an isotropic texture, with grains displaying the full range of extinction angles under crossed polars.

Serpentinite collected by the author from the south-eastern side of Rio nell'Elba (Lat, Lon: 42.80785, 10.40513) on the Isle of Elba, Italy, consists largely of lizardite ($Mg_{2.8}Fe_{0.2}Si_2O_5(OH)_4$) with minor chrysotile arranged in mesh cells and bastites on the order of 1 mm in diameter (Fig. 1b). Chrysotile may occur between the lizardite grains in the mesh rims as coatings ≤800 Å, or as fibres 300–500 Å in diameter within the mesh cores (Viti and Mellini, 1998). The specimen from Elba displays a weak anisotropy in optical microscopy, revealed by extinction angles. To avoid any orientation bias, specimens of antigorite and lizardite were cut into three orthogonal directions for analysis.

Fibrous asbestiform chrysotile was acquired from King City Asbestos Mine, New Idria, CA. Owing to the fragility of these specimens, samples were only polished parallel to the long axis of the fibres. Indents are made only on this polished face, perpendicular to the fibres.

Finally, to analyse the magnesium endmember of the chlorite group, a specimen of clinochlore was obtained from the Tilly Foster Iron Mine near Brewster, NY. Crystals of clinochlore were large (3–10 mm) with well-developed cleavage, and split easily parallel to the (001) planes. Polishing the chlorite in three orthogonal directions proved to be impossible and so the samples were polished only parallel to the (001) planes. All indents are perpendicular to the (001) plane.

Preparation of all samples for nanoindentation was performed by hand lapping using incrementally decreasing alumina grit sizes down to 0.25 μm. A final polishing step of colloidal silica was performed to ensure that the sample surface was as flat and undamaged as possible prior to mechanical testing.

2.2. Nanoindentation

Load-controlled nanoindentation testing was conducted across a range of temperatures (Lizardite: 25–275 °C; Antigorite: 25–500 °C, Chlorite: 25–400 °C, Chrysotile: 25 °C) in a Hysitron TI 950 TriboIndenter equipped with a diamond-tipped Berkovich probe and Brucker xSol high-temperature stage in the McKelvey School of Engineering at Washington University in St Louis. The temperature ranges were chosen to ensure that the samples remained below the dehydration point at all times during mechanical testing (Evans, 2004; Ulmer and Trommsdorff, 1995). Individual indentation experiments for antigorite and lizardite are comprised of an 8 second loading phase to a maximum load of 8 mN, a 2 second hold period and an 8 second unloading phase. Experiments on chlorite and chrysotile were conducted using a 5 s loading period to a maximum load of 5 mN, a 2 s hold, and a 5 s unloading period. These loading patterns ensure that each indent is sufficiently deep (200–300 nm) to prevent blunted or broken probe tips from affecting the data. Indentation strain-rate is calculated from the displacement rate of the indenter probe, normalized by the incremental displacement, and ranges in this study from $2 \times 10^{-2} - 3 \times 10^{-2}\, s^{-1}$ (see Kranjc et al., 2016 for additional details). At these conditions deformation is largely independent of strain-rate. Polycrystalline samples of antigorite and lizardite were indented using both 60 μm and 30 μm spaced overlapping grids to avoid sampling different populations of grain orientations at each temperature step. Samples of chrysotile and chlorite, which could only be polished in one orientation, were indented using 10 μm spaced grids. Owing to the self-confined nature of nanoindentation, the volume of an indent (10^{-20} m^3), and the grain size of the antigorite specimen, individual indents in the antigorite serpentinite are assumed to sample one distinct grain for each measurement. Similarly, indents in chlorite test different grains, but are all perpendicular to (001). The structure of the lizardite serpentinite is more complex, with extremely fine grained lizardite platelets (up to 0.15 μm in length) comprising the bastites and the polygonal serpentine in the mesh cores. Larger lizardite grains (3 μm x 1 μm) are present as sectors in the mesh rims (Viti and Mellini, 1998). Therefore, it is assumed that indents in the lizardite represent either a single sector grain or sample multiple lizardite platelets.

Indentation loads, P (ideal precision < 1 nN), and probe displacement, h (ideal precision < 0.02 nm), are measured simultaneously during each discrete indentation experiment in order to calculate the contact depth, h_c:

$$h_c = h - \frac{3P_{max}}{4S} \tag{1}$$

where P_{max} is the maximum load and S is the initial unloading stiffness, which is derived from the gradient of the initial section of the unloading curve. The projected contact area can then be calculated from the polynomial:

$$A_c = a_0 h_c^2 + a_1 h_c + a_2 h_c^{1/2} + a_3 h_c^{1/4} + \ldots \tag{2}$$

where a_i are constants obtained by indenting fused silica, which has a well-known indentation hardness and elastic modulus, over the range 100–10,000 μN. The indentation hardness, H, is calculated using the equation:

$$H = \frac{P_{max}}{A_c} \tag{3}$$

and the reduced elastic modulus, E_r, is computed from the formula:

$$E_r = \frac{S\sqrt{\pi}}{2\sqrt{A_c}} \tag{4}$$

The reduced modulus and the Young's modulus, E, are related by the subsequent equation:

$$\frac{1}{E_r} = \left(\frac{1-\nu^2}{E}\right)_{sample} + \left(\frac{1-\nu^2}{E}\right)_{probe} \tag{5}$$

where ν is Poisson's ratio. The Young's modulus and Poisson's ratio for the diamond probe are 1140 GPa and 0.07, respectively. See Sly et al. (2020) and Strozewski et al. (2021) for additional details on the experimental procedure and data reduction.

The shape of the load-displacement curve for each indent were visually inspected for quality control. Load-displacement curves with rapid changes in slope or sudden increases in depth greater than 100 nm are considered abnormal. Abnormal load-displacement curves may signify that the probe tip encountered an uneven sample surface, dirt, dust, or other blemish, and are therefore discarded. Examples of typical load-displacement curves are shown in Fig. 2. 25 indents were made in

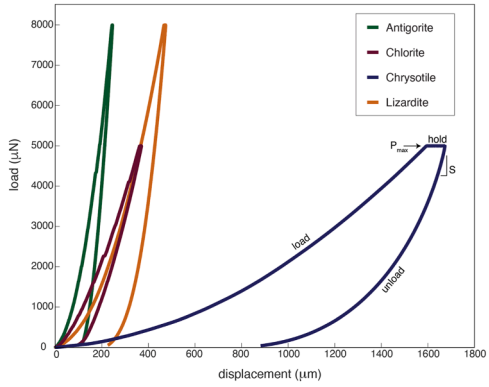

Fig. 2. Examples of Load-Displacement curves for the four minerals tested in this study. All data shown here were collected at room temperature and exhibit no anomalous jumps in displacement that would indicate a flawed measurement. Load, hold, and unload segments are labelled on the chrysotile curve, along with the maximum load (P_{max}) and the unloading stiffness (S) from Eq. (1). Weaker materials have shallower loading and unloading slopes, and exhibit a larger plateau at the maximum load, which develops during the hold stage of the test.

each of the three sample orientations for both lizardite and antigorite at each temperature step up to the maximum (a total of 75 indents per temperature increment). 49 indents were made in the surface of both the chlorite single crystal and the chrysotile at each temperature step.

3. Results

3.1. Nanoindentation

The indentation hardness of antigorite exhibits only a weak dependence on temperature across the range of antigorite stability (Table 1 and Fig. 3). There is a small decrease in the mean hardness from 6.7 to 5.7 GPa between the room temperature and 500 °C indents, respectively. The reduced elastic modulus does not change across the range of temperatures tested, remaining constant at a mean value of around 90–95 GPa. Similarly, the indentation hardness of lizardite is essentially temperature independent. Between the highest and lowest temperatures tested, mean hardnesses remain the same within error at values of 2.3–2.6 GPa. Correspondingly, the reduced elastic modulus does not vary significantly with temperature, with mean values remaining consistently in the range 38–48 GPa. Chrysotile is so weak that specimens could only be tested at room temperature, where the system could distinguish between the feedback from thermal noise and contact with the surface of the material. Hardnesses were very low and averaged 0.1 GPa. Reduced elastic moduli were also significantly lower than the other minerals tested in this study, averaging 2.0 GPa. Chlorite, unlike lizardite and antigorite, displayed a stronger dependence of strength on temperature, with a hardness of 4.0 GPa at room temperature dropping to a hardness of 2.8 GPa at 400 °C. In addition to the hardness, the reduced elastic modulus also decreased from 14.7 GPa to 6.4 GPa across the same range of temperatures. Specimens could not be tested above this temperature because, similar to the chrysotile, the samples weakened to the point that the system could not distinguish between feedback from the thermal noise and contact with the surface of the material.

3.2. Flow law fitting

The conversion from indentation hardness (H) to yield stress (σ_y), although typically written as a simple linear relationship ($H = C\sigma_y$), with C representing the constant of proportionality known as the "constraint factor" (Tabor, 1970), is a non-trivial problem due to the complex stress and strain state under a Bercovich indenter tip (Fischer-Cripps, 2004). There are various models which have been used to calculate yield stress from indentation data (e.g. Evans and Goetze, 1979; Ginder et al., 2018; Johnson, 1970; Mata and Alcalá, 2003) and from previous studies we have concluded that there is no strong empirical basis for selecting one model over the other (Sly et al., 2020; Strozewski et al., 2021). In this study, we used the model from Ginder et al., 2018 (see Sly et al., 2020 for details on this calculation) as this returned yield stresses that were the closest to existing literature estimates from Burdette and Hirth (2022) and Hilairet et al. (2007) (Table 1 and Fig. 4).

Table 1
Summary of post quality control nanoindentation data and calculated yield stress using the approach of (Ginder et al. (2018)). Errors are given as one standard deviation.

Antigorite			
T (K)	Number of indents	Mean Hardness (GPa)	Yield Stress Estimate (GPa)
298.15	72	6.67 ± 1.34	2.72
373.15	71	6.64 ± 1.18	2.70
473.15	72	6.21 ± 1.02	2.53
573.15	73	5.92 ± 0.82	2.41
673.15	73	5.73 ± 0.63	2.33
773.15	72	5.60 ± 0.72	2.28
Lizardite			
298.15	64	2.30 ± 0.40	0.94
373.15	65	2.28 ± 0.29	0.93
473.15	57	2.34 ± 0.38	0.95
548.15	43	2.28 ± 0.29	0.93
Chrysotile			
298.15	44	0.12 ± 0.02	0.12
Chlorite			
298.15	49	4.00 ± 0.71	3.63
473.15	45	2.95 ± 0.29	2.68
673.15	45	2.88 ± 0.63	2.62

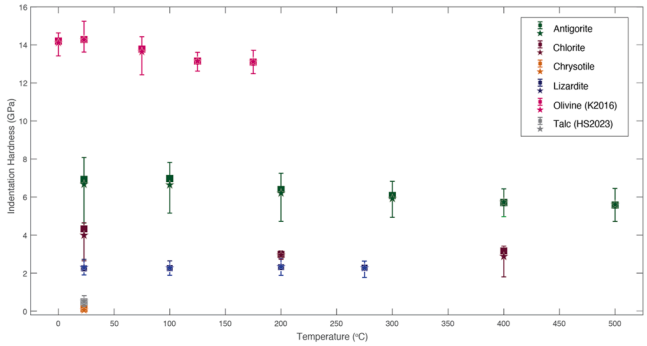

Fig. 3. Comparison of different mineral hardnesses with respect to temperature (squares = median hardness, stars = mean hardness, error bars = 10:90 percentile ranges). Olivine (data from Kranjc et al. (2016)) is harder by a factor of two than any of the hydrous magnesian silicates tested here. Antigorite is the next hardest with a small dependence of hardness on temperature. Lizardite, weaker again, shows little to no temperature dependence across the range of temperatures tested. The magnesium endmember of the chlorite group, clinochlore, has a strength between that of antigorite and lizardite but undergoes a much more pronounced weakening as temperature increases. Finally, chrysotile and talc (talc data from Horn and Skemer, 2023) are weakest at approximately two orders of magnitude lower hardness than olivine.

To fit the calculated yield stress values to a flow law, we used the approach of Sly et al. (2020), which fits values to a slightly modified version of the equation for low temperature plasticity from Frost and Ashby (1982) (see also Hansen et al., 2019):

$$\dot{\varepsilon} = A\ exp\left\{ -\frac{E^*}{RT}\left[1 - \left(\frac{\sigma_y}{\sigma_p}\right)^p\right]^q \right\} \quad (6)$$

where $\dot{\varepsilon}$ is the strain rate (i.e. the normalized change in length per unit time, with units of s^{-1}), A is the prefactor, E^* is the activation energy, R is the gas constant, T is the temperature, σ_y and σ_p are the yield and Peierls stresses, respectively, and p and q are dimensionless quantities

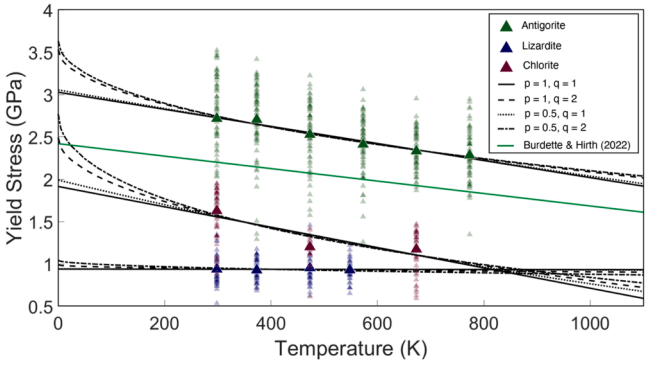

Fig. 4. Flow laws for antigorite, lizardite, and chlorite calculated using the modified flow law for low temperature plasticity from Frost and Ashby (1982). Yield stresses were computed using the Ginder et al. (2018) model for converting indentation hardness to yield stress. All indents are represented in this plot, with the mean for each respective mineral and temperature step shown as a larger solid triangle. For comparison we also show the flow law for antigorite from Burdette and Hirth (2022).

that are dependent on the obstacles that inhibit dislocation motion. The data cannot independently constrain all material-dependent unknowns (A, E^*, σ_p; see Sly, 2022) so we assume an activation energy (E^*) of 59.9 kJ/mol that was previously determined by Hilairet et al. (2007) for antigorite and fit values for A and σ_p using the MATLAB Curve Fitting Tool. Since there are no estimates for E^* in any of the other minerals besides antigorite, we use this same activation energy to fit these indentation data to a flow law. Finally, the yield stress conversion from Ginder et al. (2018) requires a value for Poisson's ratio. Values for the Poisson's ratio for antigorite (0.29) and lizardite (0.35) were taken from Christensen (2004). In the absence of a known Poisson's ratio for chlorite, the Poisson's ratio for a perfectly isotropic elastic material (0.25) was used.

4. Discussion

Nanoindentation tests the mechanical hardness of phases under conditions where crystal plasticity is favoured. These testing conditions are also similar to the conditions at the tips of rupturing cracks, where stresses and strain-rates are far greater than background conditions in the convecting mantle (Kreemer et al., 2000; Liu et al., 2018; Rice, 1992). At these conditions many hydrous minerals are markedly softer than the dominant mantle mineral, olivine. Samples of natural olivine tested in the same manner as this study by Kranjc et al. (2016) were shown to be between 2 and 3 times harder than antigorite, 6–7 times harder than lizardite and chlorite, and 100 times harder than talc and chrysotile (Fig. 3). Although the olivine samples did weaken more significantly than any serpentine variety at elevated temperatures, this weakening is not great enough to overlap with the hardnesses of any of these hydrous minerals within their relative stability fields. Chrysotile under indentation conditions is even weaker than the weakest of the Mohs scale minerals, talc (Table 1) (Broz et al., 2006; Horn and Skemer, 2023).

Samples of chlorite fall between antigorite and lizardite in terms of indentation hardness and display more pronounced weakening with respect to temperature. Since the chlorite was only tested in one orientation, perpendicular to the basal slip system, these data might be expected to represent an upper limit to the strength of chlorite. Our data are inconsistent with some previous results on the indentation hardness of chlorite, which report a lower indentation hardness of $H = 1.5$ GPa at room temperature (Liu et al., 2022). The discrepancy may be as a result of orientation differences, or due to the fact that the sample tested by Liu et al. was very fine grained and polymineralic.

As noted in prior studies and confirmed in this present study, there is wide variation in the rheological properties of the hydrous magnesium silicates. This difference is notable even between the various varieties of just the serpentine group, with lizardite yielding at lower stresses than antigorite (Escartín et al., 1997; Hirauchi and Katayama, 2013; Raleigh and Paterson, 1965) and chrysotile yielding at significantly lower stress than either of the other two varieties. We find that across the range of temperatures tested in the present study antigorite hardnesses are about 3 times larger than hardnesses determined for lizardite (Fig. 3). Neither antigorite nor lizardite displays a strong dependence of strength relative to temperature, with antigorite weakening slightly as temperature increases while lizardite strength remains temperature-independent up to close to the dehydration point. A weak dependence of strength on temperature has been observed in prior work on both these serpentine species (Amiguet et al., 2012; Hilairet et al., 2007). Although there have been no high temperature nanoindentation studies on the mineral talc, prior experimental work indicates that its rheology is largely controlled by its coefficient of friction (Escartín et al., 2008). It is therefore reasonable to assume that talc's hardness is largely independent of temperature.

Lizardite, antigorite, and chrysotile are all phyllosilicate minerals of near-identical chemistry, with the main difference being in the configuration of the sheets within the crystal structure. In lizardite, planar sheets are simply stacked one on top of another, allowing for an easy basal glide slip system. In chrysotile, these sheets are rolled into tubes and fibres, and the theoretical primary slip system is unclear. Finally, the corrugated sheets that make up the antigorite crystal structure inhibit slip on the basal planes, resulting in a conjugate glide system on the (101) and (10$\bar{1}$) crystallographic planes (Amiguet et al., 2014). Since this conjugate slip system requires the breaking of covalent bonds rather than weak hydrogen bonds in the basal plane, it follows that dislocation motion should have a lower activation energy for lizardite vs antigorite. This could help to explain the contrasting rheologies between these two serpentine species. Likewise, it is possible that the limited effect of temperature on the rheology of antigorite could also be explained by considering the structural dissimilarities. As temperature increases, it is conceivable that basal glide in antigorite becomes easier to achieve by allowing the crenelated crystal structure to overcome the energy barrier to deformation within the basal plane more readily. It has also been suggested that there is a link between the antigorite crystallographic a-axis length and thermobaric conditions, with increasing metamorphic grade resulting in a lower a-axis length (Mellini et al., 1987). This could translate into shorter Burgers vector lengths at high temperature, reducing the energy cost to crystal deformation. Alternatively, a recent study on the indentation of antigorite using a spherical tip indenter probe suggested that the deformation of antigorite under these conditions was dominated by the formation of shear cracks (Hansen et al., 2020). The authors proposed that this could be controlled by the frictional strength of interfaces. Although the frictional coefficients of lizardite and antigorite have been shown to be different (Reinen et al., 1994), the frictional coefficient of antigorite gouge remains constant with increasing temperature while the frictional coefficient of lizardite increases (Moore et al., 1997). It should also be noted that some more recent high pressure studies (Chernak and Hirth, 2010; Proctor and Hirth, 2016) have observed a reduction in the apparent friction coefficient of antigorite with increasing temperature, which may reflect the complex interplay between frictional and plastic deformation. Since our data show that antigorite strength decreases with increasing temperature while lizardite strength remains constant, and we see no macroscopic evidence for brittle deformation, we infer that the indentation hardness of the serpentine species in this study is not controlled by frictional sliding along cracks. However, more work is needed to understand the microphysics of serpentine deformation and to correlate mechanisms with mechanical data.

Unlike antigorite and lizardite, chlorite displays a more pronounced dependence on temperature and is projected to decrease to a hardness equivalent to lizardite by ~550–600 °C. Given the larger stability field of chlorite compared to the serpentine group (Evans, 2004; Pawley, 2003; Ulmer and Trommsdorff, 1995), chlorite should continue to have a pronounced weakening effect on subducting material to much greater depths than the serpentine group minerals. In the same way, talc, which is also stable to higher temperatures than the serpentine group (Pawley and Wood, 1995), should be important rheologically across a wide pressure-temperature space.

When the indentation hardness for each of these phyllosilicate minerals is plotted against the c-spacing, there is a general trend of weakening with increasing space between the lattice planes (Amiguet et al., 2014; Ross et al., 1968; Rule and Bailey, 1987) (Fig. 5). We hypothesize that, as the distance between lattice planes increases, the easier it becomes to deform by slip in the basal plane. Since basal slip is effectively the only slip system in these layered silicates, we suggest that the c-spacing effectively controls the mineral rheology. This trend is violated somewhat in the case of antigorite, which has c-spacing similar to lizardite, but we speculate that the corrugated nature of the crystallographic sheets act to impede basal slip and strengthen the antigorite relative to non-corrugated phases (Amiguet et al., 2014). It is also unclear how c-spacing should affect the rheology of chrysotile, since

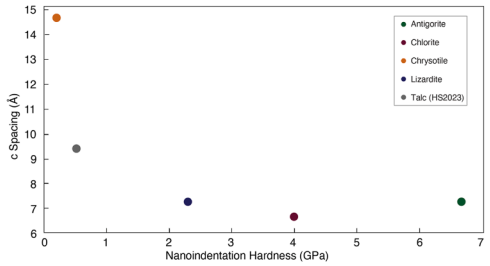

Fig. 5. c-spacing vs hardness for each of the phyllosilicate minerals discussed in this study, from chrysotile (weakest) to antigorite (strongest). Lattice spacings were obtained from Amiguet et al. (2014) (antigorite and lizardite), Falini et al. (2004) (chrysotile), Ross et al. (1968) (talc), and Rule and Bailey (1987) (chlorite).

individual sheets are rolled into fibres/cylinders. In the case of chrysotile occurring with well aligned fibres, it might be expected that the chrysotile is deforming by slip of the individual fibres with respect to one another rather than intragranular deformation mechanisms.

Although the result of this study confirm that these hydrous magnesium silicates are significantly weaker than many other minerals, the calculated yield strengths (Table 1) are greater than those found in other studies (Fig. 4) (Amiguet et al., 2012; Burdette and Hirth, 2022; Hilairet et al., 2007). There are several possible reasons for this. It has previously been shown in olivine that the apparent strength of a mineral may depend on the length scale over which that mineral is deformed (Kumamoto et al., 2017). Since nanoindentation involves volumes on the order of about 10^{-20} m^3, it might be expected that it should appear stronger than experiments performed on mm to cm-scale samples. However, size effects are dependent on the availability of slip systems within a crystal lattice. As hydrous phyllosilicates are not expected to have many viable slip systems and therefore must take up additional strain via alternative deformation mechanisms such as comminution along grain boundaries (Amiguet et al., 2014) or ripplocations (Aslin et al., 2019), any strength disparity due to differences in observational length scales may be suppressed. An alternative solution is that the difference in strength arises from the fact that grain boundaries may play a much larger role in the deformation of polycrystalline samples (Amiguet et al., 2012; Burdette and Hirth, 2022; Hilairet et al., 2007) than in the small-volume indentation experiments. However, while this may be true for the antigorite where indents can be comfortably assumed to sample individual grains, this theory does not hold for lizardite as its fine grain sizes (see Methods) mean that indents likely sample multiple grains, yet still produce greater yield stresses than prior studies (Amiguet et al., 2012), even when extrapolated to the same strain rates. Regardless of the exact cause for this discrepancy, we consider our results to be an upper limit to the yield strengths of the serpentine minerals and chlorite.

The overall weakness of all the hydrous magnesium silicates tested in this study indicates that, as previously surmised, phyllosilicate minerals are likely to be very important for localising strain at conditions within their stability fields (e.g. Hirth and Guillot (2013); Reynard (2013), and references therein). As the oceanic lithosphere becomes hydrated, it is most likely to alter first to form lizardite, the most common hydrous mineral on the seafloor (Christensen, 1972; Ulmer and Trommsdorff, 1999; Wicks and Whittaker, 1977). During subsequent prograde metamorphism at convergent margins, antigorite forms either by the replacement of lizardite (O'Hanley and Wicks, 1995), or directly as a result of fluid infiltration into ultramafic materials (Peacock, 1987). Chrysotile appears to be universally metastable, and is found most frequently in isotropic stress microenvironments within regions of otherwise high tectonic stress (Evans, 2004). Talc and chlorite typically occur in much lower abundance than the serpentine minerals (Boschi et al., 2006; Moore and Rymer, 2007; Spandler et al., 2008) and form from the interaction of metasomatic fluids with either serpentinite bodies (Hirauchi et al., 2020; King et al., 2003; Spandler et al., 2008) or dolomites (Puhan and Hoffer, 1973). Despite this, both talc and chlorite are stable over a much wider range of temperatures than any of the serpentine species and are expected to persist deeper into a subduction zone (Spandler et al., 2008) (Table 2). Since these weak, hydrous phases are widespread in the shallow oceanic lithosphere, it naturally follows that the formation/propagation of faults and shear zones should be enhanced by the presence of these phases (Hirauchi et al., 2016; Kohli et al., 2021). In particular, it is possible that, under the right conditions, one of those weakened faults or shear zones could become enhanced to the point that the buoyantly unstable oceanic lithosphere is able to break off and subside into the mantle (Izumi et al., 2023; Reynard, 2013).

The wide range of ages over which modern day trenches can be dated indicates that the formation of subduction zones is relatively easy (Stern and Gerya, 2018). Various processes have been suggested to explain subduction initiation, yet the dominant mechanism(s) remain unclear and we continue to be reliant on numerical modelling to probe developments that occur over millions of years (Stern and Gerya, 2018). As dry olivine is evidently too strong to allow the lithosphere to be breached under normal conditions (Hirth and Kohlstedt, 2003), a common feature of many geodynamic models is the existence of a weak zone that can be exploited by the nascent subduction zone (Dymkova and Gerya, 2013; Nikolaeva et al., 2010; Toth and Gurnis, 1998). Although weakening by hydrous phases has been explored as an alternative option for subduction initiation (Gerya et al., 2008), the nuances of fault zone weakening by hydrous reaction products are rarely explored by numerical modelling for the sake of computational simplicity. Instead, numerical models often take a real "weak" rheology (e.g. "wet olivine" Nikolaeva et al. (2010)) or a hypothetical viscosity contrast (e.g. Toth and Gurnis (1998)) to simulate weakening in the lithosphere prior to subduction initiation. This approach, while both practical and useful, overlooks crucial details of lithospheric weakening by hydrous phases. As documented in this study, there are marked contrasts in the strength of all these (chemically very similar) hydrous phases (Fig. 3). Therefore, it makes a significant difference which phase is present. The occurrence of water saturated but nominally anhydrous olivine may already reduce mantle viscosity by several orders of magnitude (Hirth and Kohlstedt, 2003), but the effect of weak hydrous phases may be even more important. Future geodynamic models may wish to further explore the enhanced weakening of the lithosphere by these critical phases.

5. Conclusions

Nanoindentation experiments on hydrous magnesium silicate minerals confirm that these minerals are orders of magnitude weaker than the dominant mantle mineral, olivine. Among these minerals, antigorite is the strongest with a mean hardness (5.7–6.7 GPa) over a wide temperature range, approximately half that of dry olivine (13.1–14.9 GPa) (Kranjc et al., 2016). Lizardite is weaker again with a mean hardness of 2.3–2.6 GPa, similar to chlorite (2.6–3.6 GPa), while chrysotile is the

Table 2
Stability fields of the hydrous magnesium silicates covered by this study. P and T refer to pressure and temperature, respectively.

Mineral	P,T coordinates for highest T	P,T coordinates for highest P	Citation(s)
Antigorite	2.1 GPa, 730 °C	~7.5 GPa, 300 °C	Ulmer and Trommsdorff (1995), Reynard (2013))
Lizardite	Atm P, 300–350 °C	Unknown, at least 0.3 GPa, 300 °C	Evans (2004), Normand et al. (2002)
Chrysotile	metastable	metastable	Evans (2004)
Chlorite	2.5 GPa, 860–880 °C	~5.0 GPa, 650 °C	Pawley (2003)
Talc	2.90–2.95 GPa, 800–820 °C	3.77–4.02 GPa, 770–780 °C	Pawley and Wood (1995)

weakest of all with a mean hardness of 0.1 GPa. Even between these chemically similar hydrous phases there is an order of magnitude difference in the hardnesses of the strongest (antigorite) and weakest (chrysotile) phases. Nevertheless, all of these minerals are still extremely weak in comparison to nominally anhydrous mantle silicates and could contribute to the initiation of subduction by facilitating localised weakening of dense oceanic lithosphere.

CRediT authorship contribution statement

Charis M. Horn: Writing – original draft, Methodology, Investigation, Formal analysis. **Philip Skemer:** Writing – review & editing, Supervision, Funding acquisition, Conceptualization.

Declaration of competing interest

The authors declare that they have no known competing financial interests or personal relationships that could have appeared to influence the work reported in this paper.

Acknowledgements

We would like to thank Jessica Warren for providing the chrysotile specimen, Kate Padilla and Suzanne Russo (nanoindenter), and Paul Carpenter (microprobe) for lending their technical expertise and assistance, Mike Sly for sharing his codes for reducing nanoindentation data, and Katharine Flores for use of the nanoindentation facility. Ken-ichi Hirauchi and an anonymous reviewer are thanked for their input. Some instrument support was provided by the Institute of Materials Science and Engineering at Washington University in St Louis. This research was supported by NSF grant EAR-1848824 to Skemer.

Data availability

Data will be made available on request.

References

Amiguet, E., Moortèle, B., Cordier, P., Hilairet, N., Reynard, B., 2014. Deformation mechanisms and rheology of serpentines in experiments and in nature. J. Geophys. Res. Solid Earth 119, 4640–4655. https://doi.org/10.1002/2013JB010791.

Amiguet, E., Reynard, B., Caracas, R., de Moortèle, B., Hilairet, N., Wang, Y., 2012. Creep of phyllosilicates at the onset of plate tectonics. Earth Planet. Sci. Lett. 345–348, 142–150. https://doi.org/10.1016/j.epsl.2012.06.033.

Aslin, J., Mariani, E., Dawson, K., Barsoum, M.W., 2019. Ripplocations provide a new mechanism for the deformation of phyllosilicates in the lithosphere. Nat. Commun. 10, 1–9. https://doi.org/10.1038/s41467-019-08587-2.

Boschi, C., Früh-Green, G.L., Escartín, J., 2006. Occurrence and significance of serpentinite-hosted, talc- and amphibole-rich fault rocks in modern oceanic settings and ophiolite complexes: an overview. Ofioliti 31, 129–140.

Broz, M.E., Cook, R.F., Whitney, D.L., 2006. Microhardness, toughness, and modulus of Mohs scale minerals. Am. Mineral. 91, 135–142. https://doi.org/10.2138/am.2006.1844.

Burdette, E., Hirth, G., 2022. Creep rheology of antigorite: experiments at subduction zone conditions. J. Geophys. Res. Solid Earth 127, 1–11. https://doi.org/10.1029/2022JB024260.

Chernak, L.J., Hirth, G., 2010. Deformation of antigorite serpentinite at high temperature and pressure. Earth Planet. Sci. Lett. 296, 23–33. https://doi.org/10.1016/j.epsl.2010.04.035.

Christensen, N., 2004. Serpentinites, peridotites, and seismology. Int. Geol. Rev. 46, 795–816. https://doi.org/10.2747/0020-6814.46.9.795.

Christensen, N., 1972. The Abundance of serpentinites in the oceanic crust. J. Geol. 80, 709–719.

Dymkova, D., Gerya, T., 2013. Porous fluid flow enables oceanic subduction initiation on Earth. Geophys. Res. Lett. 40, 5671–5676. https://doi.org/10.1002/2013GL057798.

Escartín, J., Andreani, M., Hirth, G., Evans, B., 2008. Relationships between the microstructural evolution and the rheology of talc at elevated pressures and temperatures. Earth Planet. Sci. Lett. 268, 463–475. https://doi.org/10.1016/j.epsl.2008.02.004.

Escartín, J., Hirth, G., Evans, B., 1997. Nondilatant brittle deformation of serpentinites: implications for Mohr-Coulomb theory and the strength of faults. J. Geophys. Res. Solid Earth 102, 2897–2913. https://doi.org/10.1029/96JB02792.

Evans, B., 2004. The serpentinite multisystem revisited: chrysotile is metastable. Int. Geol. Rev. https://doi.org/10.2747/0020-6814.46.6.479.

Evans, B., Goetze, C., 1979. The temperature variation of hardness of olivine and its implication for polycrystalline yield stress. J. Geophys. Res. 84.

Evans, B., Johannes, W., Oterbom, H., Trommsdroff, V., 1976. Stability of chrysotile and antigorite in the serpentine multisystems. Schweiz. Mineral. Petrogr. 56, 79–93.

Falini, G., Foresti, E., Gazzano, M., Gualtieri, A.E., Leoni, M., Lesci, I.G., Roveri, N., 2004. Tubular-shaped stoichiometric chrysotile nanocrystals. Chem. A Eur. J. 10, 3043–3049. https://doi.org/10.1002/chem.200305685.

Fischer-Cripps, A., 2004. Nanoindentation, Mechanical Engineering Series. Springer Science+Business Media, LLC. https://doi.org/10.1115/1.1704625.

Frost, H.J., Ashby, M.F., 1982. Deformation-mechanism maps: The plasticity and Creep of Metals and Ceramics. Pergamon Press.

Gerya, T.V., Connolly, J.A.D., Yuen, D.A., 2008. Why is terrestrial subduction one-sided? Geology 36, 43–46. https://doi.org/10.1130/G24060A.1.

Ginder, R.S., Nix, W.D., Pharr, G.M., 2018. A simple model for indentation creep. J. Mech. Phys. Solids. 112, 552–562. https://doi.org/10.1016/j.jmps.2018.01.001.

Hansen, L.N., David, E.C., Brantut, N., Wallis, D., 2020. Insight into the microphysics of antigorite deformation from spherical nanoindentation. Philos. Trans. R. Soc. A Math. Phys. Eng. Sci. 378. doi:10.1098/rsta.2019.0197.

Hansen, L.N., Kumamoto, K.M., Thom, C.A., Wallis, D., Durham, W.B., Goldsby, D.L., Breithaupt, T., Meyers, C.D., Kohlstedt, D.L., 2019. Low-Temperature plasticity in olivine: grain size, strain hardening, and the strength of the lithosphere. J. Geophys. Res. Solid Earth 124, 5427–5449. https://doi.org/10.1029/2018JB016736.

Hilairet, N., Reynard, B., Wang, Y., Daniel, I., Merkel, S., Nishiyama, N., Petitgirard, S., Nishiyama, N., Petitgirard, S., 2007. High-Pressure creep of serpentine, interseismic deformation, and initiation of subduction. Science (1979) 318, 1910–1913. https://doi.org/10.1126/science.1148494.

Hirauchi, K., Fukushima, K., Kido, M., Muto, J., Okamoto, A., 2016. Reaction-induced rheological weakening enables oceanic plate subduction. Nat. Commun. 7, 1–7. https://doi.org/10.1038/ncomms12550.

Hirauchi, K.ichi, Katayama, I., 2013. Rheological contrast between serpentine species and implications for slab-mantle wedge decoupling. Tectonophysics. 608, 545–551. https://doi.org/10.1016/j.tecto.2013.08.027.

Hirauchi, K., Yamamoto, Y., den Hartog, S.A.M., Niemeijer, A.R., 2020. The role of metasomatic alteration on frictional properties of subduction thrusts: an example from a serpentinite body in the Franciscan Complex, California. Earth Planet. Sci. Lett. 531, 115967. https://doi.org/10.1016/j.epsl.2019.115967.

Hirth, G., Guillot, S., 2013. Rheology and tectonic significance of serpentinite. Elements 9, 107–113. https://doi.org/10.2113/gselements.9.2.107.

Hirth, G., Kohlstedt, D., 2003. Rheology of the upper mantle and the mantle wedge: a view from the experimentalists upper mantle. Inside the subduction factory. Geophys. Monogr. 138, 83–105.

Horn, C., Bouilhol, P., Skemer, P., 2020. Serpentinization, deformation, and seismic anisotropy in the subduction mantle wedge. Geochem. Geophys. Geosyst. 21, 1–17.

Horn, C., Skemer, P., 2023. Semi-Brittle deformation of talc at the base of the seismogenic zone. J. Geophys. Res. 50, 1–9. https://doi.org/10.1029/2022GL102385.

Izumi, M., Hirauchi, K.ichi, Yoshida, M., 2023. Mantle-wedge alteration facilitates intra-oceanic subduction initiation along a pre-existing fault zone. Tectonophysics 861. https://doi.org/10.1016/j.tecto.2023.229908.

Johnson, K.L., 1970. The correlation of indentation experiments. J. Mech. Phys. Solids 18, 115–126. https://doi.org/10.1016/0022-5096(70)90029-3.

King, R.L., Kohn, M.J., Eiler, J.M., 2003. Constraints on the petrologic structure of the subduction zone slab-mantle interface from Franciscan Complex exotic ultramafic blocks. Geol. Soc. Am. Bull. 115, 1097–1109.

Kohli, A., Wolfson-Schwehr, M., Prigent, C., Warren, J.M., 2021. Oceanic transform fault seismicity and slip mode influenced by seawater infiltration. Nat. Geosci. 14, 606–611. https://doi.org/10.1038/s41561-021-00778-1.

Kranjc, K., Rouse, Z., Flores, K., Skemer, P., 2016. Low-temperature plastic rheology of olivine determined by nanoindentation. Geophys. Res. Lett. 43, 176–184. https://doi.org/10.1002/2015GL065837.

Kreemer, C., Haines, J., Holt, W.E., Blewitt, G., Lavallee, D., 2000. On the determination of a global strain rate model. Earth Planets Space 52, 765–770.

Kumamoto, K.M., Thom, C.A., Wallis, D., Hansen, L.N., Armstrong, D.E.J., Warren, J.M., Goldsby, D.L., Wilkinson, A.J., 2017. Size effects resolve discrepancies in 40 years of work on low-temperature plasticity in olivine. Sci. Adv. 3, 1–7. https://doi.org/10.1126/sciadv.1701338.

Liu, J., Wang, J., Wan, W., 2018. Numerical study of crack propagation in an indented rock specimen. Comput. Geotech. 96, 1–11. https://doi.org/10.1016/j.compgeo.2017.10.014.

Liu, Y., Liu, A., Liu, S., Kang, Y., 2022. Nano-scale mechanical properties of constituent minerals in shales investigated by combined nanoindentation statistical analyses and SEM-EDS-XRD techniques. Int. J. Rock Mech. Min. Sci. 159. https://doi.org/10.1016/j.ijrmms.2022.105187.

Mata, M., Alcalá, J., 2003. Mechanical property evaluation through sharp indentations in elastoplastic and fully plastic contact regimes. J. Mater. Res. 18, 1705–1709. https://doi.org/10.1557/JMR.2003.0234.

Mellini, M., Trommsdorff, V., Compagnoni, R., 1987. Antigorite polysomatism: behaviour during progressive metamorphism. Contrib. Mineral. Petrol. 97, 147–155. https://doi.org/10.1007/BF00371235.

Mével, C., 2003. Serpentinization of abyssal peridotites at mid-ocean ridges 335, 825–852.

Moore, D.E., Lockner, D.A., Shengli, M., Summers, R., Byerlee, J.D., Lockner, J.D., Ma, S., Summers, R., Byerlee, J.D., 1997. Strengths of serpentinite gouges at elevated temperatures. J. Geophys. Res. 102, 14787–14801.

Moore, D.E., Rymer, M., 2007. Talc-bearing serpentinite and the creeping section of the San Andreas fault. Nature 448, 795. https://doi.org/10.1038/nature06064.

Nikolaeva, K., Gerya, T.V., Marques, F.O., 2010. Subduction initiation at passive margins: numerical modeling. J. Geophys. Res. Solid Earth 115, 1–19. https://doi.org/10.1029/2009JB006549.
Normand, C., Williams-Jones, A.E., Martin, R.F., Vali, H., 2002. Hydrothermal alteration of olivine in a flow-through autoclave: nucleation and growth of serpentine phases. Am. Mineral. 87, 1699–1709.
O'Hanley, D.S., Wicks, F.J., 1995. Conditions of formation of lizardite, chrysotile and antigorite, Cassiar, British Columbia. Can. Mineral. 33, 753–773.
Parai, R., Mukhopadhyay, S., 2012. How large is the subducted water flux? New constraints on mantle regassing rates 317, 396–406. doi:10.1016/j.epsl.2011.11.024.
Pawley, A., 2003. Chlorite stability in mantle peridotite: the reaction clinochlore+enstatite=forsterite+pyrope+H2O. Contrib. Mineral. Petrol. 144, 449–456. https://doi.org/10.1007/s00410-002-0409-y.
Pawley, A., Wood, B.J., 1995. The high-pressure stability of talc and 10 Å phase: potential storage sites for H2O in subduction zones. Am. Mineral. 80, 998–1003. https://doi.org/10.2138/am-1995-9-1015.
Peacock, S.M., 1987. Serpentinization and infiltration metasomatism in the Trinity peridotite, Klamath province, northern California: implications for subduction zones. Contrib. Mineral. Petrol. 95, 55–70. https://doi.org/10.1007/BF00518030.
Proctor, B., Hirth, G., 2016. "Ductile to brittle" transition in thermally stable antigorite gouge at mantle pressures. J. Geophys. Res. Solid Earth 121, 1652–1663. https://doi.org/10.1002/2015JB012710.
Puhan, D., Hoffer, E., 1973. Phase relations of talc and tremolite in metamorphic calcite-dolomite sediments in the southern portion of the Damara Belt (South West Africa). Contrib. Mineral. Petrol. 40, 207–214. https://doi.org/10.1007/BF00373785.
Raleigh, C., Paterson, M., 1965. Experimental deformation of serpentinite and its tectonic implications. J. Geophys. Res. 70, 3965–3985. https://doi.org/10.1029/JZ070i016p03965.
Reinen, L.A., Weeks, J.D., Tullis, T.E., 1994. The frictional behavior of lizardite and antigorite serpentinites: experiments, constitutive models, and implications for natural faults. Pure Appl. Geophys. 143, 317–358. https://doi.org/10.1007/BF00874334.
Reynard, B., 2013. Serpentine in active subduction zones. Lithos 178, 171–185. https://doi.org/10.1016/j.lithos.2012.10.012.
Rice, J.R., 1992. Dislocation nucleation from a crack tip: an analysis based on the Peierls concept. J. Mech. Phys. Solids 40, 239–271.
Ross, M., Smith, W.L., Ashton, W.H., 1968. Triclinic talc and associated amphiboles from Gouverneur Mining District, New York. Am. Mineral. 53, 751–769.
Rule, A.C., Bailey, S.W., 1987. Refinement of the crystal structure of a monoclinic ferroan clinochlore. Clays. Clay. Miner. 35, 129–138.
Rüpke, L., Morgan, J., Hort, M., Connolly, J., 2004. Serpentine and the subduction zone water cycle. Earth Planet. Sci. Lett. 223, 17–34. https://doi.org/10.1016/j.epsl.2004.04.018.
Sly, M.K., 2022. Low-Temperature Plasticity of Rock-Forming Minerals. Washington University in St. Louis.b.
Sly, M.K., Thind, A.S., Mishra, R., Flores, K.M., Skemer, P., 2020. Low-temperature rheology of calcite. Geophys. J. Int. 221, 129–141. https://doi.org/10.1093/gji/ggz577.
Spandler, C., Hermann, J., Faure, K., Mavrogenes, J.A., Arculus, R.J., 2008. The importance of talc and chlorite "hybrid" rocks for volatile recycling through subduction zones; evidence from the high-pressure subduction mélange of New Caledonia. Contrib. Mineral. Petrol. 155, 181–198. https://doi.org/10.1007/s00410-007-0236-2.
Stern, R.J., Gerya, T., 2018. Subduction initiation in nature and models: a review. Tectonophysics 746, 173–198. https://doi.org/10.1016/j.tecto.2017.10.014.
Strozewski, B., Sly, M.K., Flores, K.M., Skemer, P., 2021. Viscoplastic rheology of α-quartz investigated by nanoindentation. J. Geophys. Res. Solid Earth 126, 1–14. https://doi.org/10.1029/2021JB022229.
Tabor, D., 1970. The hardness of solids. Rev. Phys. Technol. 1.
Toth, J., Gurnis, M., 1998. Dynamics of subduction initiation at preexisting fault zones. J. Geophys. Res. 103, 18053–18067.
Ulmer, P., Trommsdorff, V., 1999. Phase relations of hydrous mantle subducting to 300km. Mantle petrology: field observations and high-pressure experimentation 6, 259–281.
Ulmer, P., Trommsdorff, V., 1995. Serpentine stability to mantle depths and subduction-related magmatism. Science (1979) 268, 858–861. https://doi.org/10.1126/science.268.5212.858.
Viti, C., Mellini, M., 1998. Mesh textures and bastites in the Elba retrograde serpentinites. Eur. J. Mineral. 10, 1341–1359.
Whittaker, E.J.W., 1957. The structure of chrysotile. V. Diffuse reflexions and fibre texture. Acta Crystallogr. 10, 149–156. https://doi.org/10.1107/s0365110x57000511.
Wicks, F.J., Whittaker, E.J.W., 1977. Serpentine Textures and Serpentinization. Can. Mineral. 15, 459–488.